Flow Assisted Evaporative Cooling for Electric Motor

Amitav Tikadar, *Student Member, IEEE*, Joon W. Kim, *Student Member, IEEE,* Yogendra Joshi, *Fellow, IEEE*, and Satish Kumar, *Senior Member, IEEE*

Abstract

This paper examines a novel concept of flow assisted latent heat driven two-phase evaporative cooling (EC) confined in-between slot liner and active-winding of electric motor. Wicking micro-structure enhanced PDMS liner axially sucks coolant in the form of thin film between the PDMS liner and active-winding and eventually enables thin film evaporation on the outer surface of the active-winding. Therefore, EC based thermal management eliminates contact resistance between the winding and slot-liner and, enhances the heat extraction from the winding without compromising the electro-magnetic performance. Two-way coupled electro-magnetic (EM) – computational fluid dynamics/heat transfer (CFD/HT) and EM - lumped parameter thermal network (LPTN) models have been developed to assess the electro-thermal performance of the EC under steady and transient conditions. Taking a case study of a 125 kW jacket cooled BMW i3 motor and dielectric coolant FC-84, EC is shown to be capable of handling a maximum steady state rms current density of 26 A/mm^2 at a evaporative heat transfer coefficient of 5,000 W/m^2.K, which is about 78.7% higher compared to the traditional jacket cooling (JC). In case of EC, a maximum steady state and transient rms current density of 30 A/mm^2 (106.2% higher compared to the JC), and 40.8 A/mm^2 have been realized by using high thermal conductivity epoxy (1.9 W/m.K) impregnation material. Thermal performance of the EC is also assessed and compared with JC over a dynamic drive cycle. Finally, a motorette testing has been performed to demonstrate the applicability of the proposed EC method and to validate the developed modeling framework.

Keywords- PMSM, slot-liner, evaporative cooling, thermal resistance, LPTN model.

I. Introduction

Stringent greenhouse gas emission legislations have accelerated the need for electrification of ground and air transportation. Since electric machines are one of the core component of the electric drivetrain, improvement of their performance is a key enabler of better performance metrics of electric drivetrain. These performance metrics include higher power and torque density, better fuel economy (lower $/mile), and overall drivetrain efficiency. Permanent magnet synchronous motors (PMSM) are broadly used in traction powertrain because of their superior performance on these metrics [1]. However, high heat generation in PMSM, especially at high power density, as a consequence of electro-magnetic losses, limits motor efficiency and longevity by ultimate aging of the winding wire insulation and premature demagnetization of the magnets. Therefore, enhanced cooling technology is essential to increase motor power and torque density, by pushing up the current density, while keeping the peak winding temperature below the winding insulation temperature threshold, without compromising efficiency.

For low power density electric machines, typically air cooling is used whereas for high power density electric motor, indirect liquid cooling is needed [2]. Typically, in automotive and industrial machines, closed loop liquid cooling via an external cooling jacket is utilized [3, 4]. However, jacket cooling (JC) technology often suffers from poor heat extraction from the winding to the external coolant because of the multiple thermal resistances between the winding and the coolant.

The thermal resistance between the winding and the coolant can be significantly reduced by placing the cooling channel directly in the stator, as discussed in [5, 6]. However, cooling channel in stator lamination can alter the magnetic flux path by imposing extra reluctances [6]. By realizing the aforementioned limitations of the JC and direct stator cooling, Semidey and Mayor [7] proposed a water cooled direct winding heat exchanger (DWHX) concept to extract heat directly from the winding. DWHX dramatically reduces the thermal resistances between the winding and the coolant, and hence significantly higher current density can be achieved, while operating within the insulation's thermal limit. After the pioneering work of Semidey and Mayor [7], effectiveness of the DWHX has been reported by many other researcher [8, 9]. Recent improvement in 3D printing technology enable the fabrication of complex DWHX geometry along with internal flow channels to further improve the efficacy of DWHX [10]. However, DWHX reduces the cooper fill factor by occupying slot area, which eventually results in high copper loss and DWHX is only applicable in concentrated wound machines. Moreover, for water cooled DWHX, proper sealing needs to be ensured for safe operation. Water can be replaced by oil/dielectric coolant to minimize the water leakage risk, at the expense of poor thermal and hydraulic performances [11]. Lindh et al. [11] replaced the centermost conductor bunch in a standard Litz wire bundle of a tooth-coil axial-flux permanent-magnet motor by axial stainless steel cooling channel. Although axial cooling channel significantly reduces the machine temperature, the fabrication of Litz wire bundle with axial cooling channel adds complexity. Rhebergen et al. [12] used axial cooling channel in the bottom of the stator slot of a switched reluctance motor and also applied enhanced polymer composite as potting material to reduce the thermal resistance between the winding and the cooling channel. However, the potting material thermal resistance can be significant.

In conventional external jacket cooled motor, end-windings are commonly identified as motor hot-spot because of

Manuscript received; revised; accepted August 11, 2021. The information, data, or work presented herein was funded in part by the Advanced Research Projects Agency-Energy (ARPA-E), U.S. Department of Energy, under Award Number DE-AR0001023 in the OPEN 2018 program monitored by Dr. Michael Ohadi and Dr. Peter de Bock. The views and opinions of authors expressed herein do not necessarily state or reflect those of the United States Government or any agency thereof. (Corresponding author: Satish Kumar).

All authors are with the G.W. Woodruff School of Mechanical Engineering, Georgia Institute of Technology, Atlanta, GA, USA, 30332. (e-mail: atikadar3@gatech.edu, jwkim9225@gatech.edu, yogendra.joshi@me.gatech.edu, and satish.kumar@me.gatech.edu)

the limited heat dissipation through the air gap between the end-winding and the housing where cooling ducts are located. Madonna et al. [13] placed a liquid-carrying plastic pipe in the end-windings to reduce the thermal resistance between the end-winding and the coolant and hence, the hot-spot temperature. However, this end-winding cooling technique often suffers from increased end-winding length, resulting in increased copper loss and contact resistance between the end-winding and the coolant carrying pipe. Nategh et al. [14] applied thermally conductive potting material (3.5 W/m.K) in the end-space to provide a direct conductive heat transfer path between the end-winding and the external cooling channel. However, the application of potting material in large size traction motors is challenging and additional weight of the potting material results in lower specific output power and torque [15].

Latent heat driven two-phase cooling technique, in particular heat pipe has also been used for high power density electric motor thermal management. As proposed in [16], evaporator section of the heat pipe can be placed directly in the stator slot, while condenser section can be axially extended beyond the stator, up to a cooling chamber/air heat exchanger. Lower copper fill factor and risk of heat pipe leakage are the major drawbacks of the aforementioned cooling techniques. Evaporator section of the heat pipe can also be placed inside the rotor/shaft as explained in [17] but this concept suffers from high risk of heat pipe damage, especially at high rotational speed. Oil spray cooling is another two-phase cooling technique commonly used for the end-winding cooling [18]. Although high heat transfer coefficient and consequently, uniform end-winding temperature can be achieved by employing spray cooling, high pumping power requirement offset the thermal benefits of the spray cooling.

In light of the above literature survey, one can conclude that close placement of cooling medium to the winding, i.e., DWHX is one of the most viable thermal management technique. However, low copper fill factor, high losses, high winding-liner and liner-lamination contact resistances, high manufacturing complexity, and limited application in concentrated wound machines often outweigh the thermal benefit of single-phase DWHX. In this paper, we have proposed a novel flow assisted thin film EC technique confined between the slot liner and active-winding of electric motor. EC in the interfacial region between the liner and active-winding can be utilized to extract heat directly from the winding without altering the winding configurations, i.e., copper fill factor, unlike direct slot cooling. Two-way coupled EM – computational fluid dynamics (CFD)/heat transfer (HT) simulations have been performed to demonstrate the effectiveness of the EC over conventional JC for a BMW i3 motor. A computationally efficient 3D lumped parameter thermal network (LPTN) model has also been developed to capture the electro-thermal performance of EC under steady-state and transient conditions. This paper is organized as follows: Section II describes the EC concept, Section III outlines the conventional BMW i3 motor topology, Section IV discusses the EM, CFD/HT simulation, and LPTN model development, Section V illustrates model validation, Section VI presents the EM and thermal performance of JC and EC over steady-state, transient, and dynamics loading (drive cycle) conditions, Section VII explains motorette testbed fabrication, testing, and CFD/HT model validation and lastly, Section VIII concludes the paper.

II. Evaporative Cooling (EC)

As mentioned earlier, this paper proposes a novel heat extraction technique from the winding via thin film EC between the slot liner and active-winding, as shown in the Fig. 1. In high power density electric motor, heat losses are generated in the windings in the form of resistive heating. In JC, heat needs to flow from the winding to the external coolant via stator tooth, back iron, and finally the housing. Additionally, winding-liner, liner-tooth/back iron, and stator lamination-housing contact resistances [19] increase the overall thermal resistance between the winding and the coolant. This long resistance chain can create hotspots inside the winding.

Micro-wicking structure can be easily printed on the surface of flexible polymers such as polydimethylsiloxane (PDMS) [20] and used as liner material in the electric motor. Wick enhanced PDMS liner need to be inserted in slots in such a way that wick micro-structure wraps active-winding. Hence, channel structure will be created between the active-winding and the PDMS liner. Utilizing capillary effect of the wick micro-structure, coolant, in the form of thin film, can be sucked and flowed axially through the channel structure between the active-winding and wick enhanced PDMS liner as shown in the Fig. 1 (b). Thin film evaporation confined between the liner and active-winding, i.e., evaporation directly outside of the active-winding, can significantly reduce the thermal resistance between the winding and the coolant by eliminating the winding-liner contact resistance, and hence can enhance the heat extraction from the winding. EC can also take advantage of high latent of vaporization, and heat transfer (contact) area between the winding and liner. Another major advantage of the EC is that it can be employed irrespective of the winding configurations. It is worth underlining that compared to the JC and DWHX, latent heat driven EC can significantly reduce the pumping power requirement by lowering the coolant flow rates, and utilizing capillary action of the wick. However, in order to implement EC in traction motor, stator sleeve may need to be used to prevent any coolant leaking from the stator slots to the rotor. Additionally, some especial coolant delivery arrangement, i.e., coolant reservoir and endcap may need to be used which may increase the complexity, weight, and volume of the evaporative cooled motor.

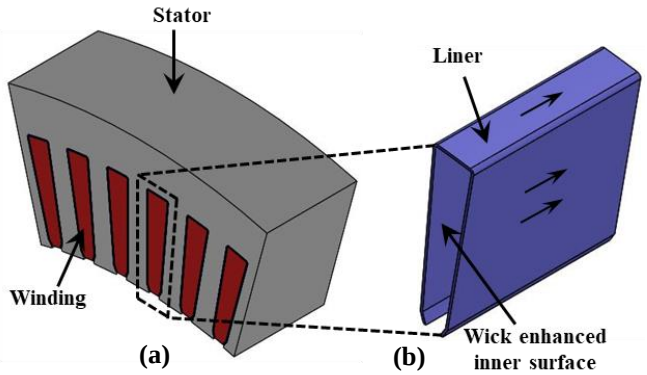

Figure 1: (a) Isometric view of the stator-winding-liner assembly, and (b) schematic of the coolant flow through liner, which is placed all around the slot.

This article has been accepted for publication in a future issue of this journal, but has not been fully edited. Content may change prior to final publication. Citation information: DOI 10.1109/TTE.2021.3107505, IEEE Transactions on Transportation Electrification

III. Motor Topology

In order to demonstrate the effectiveness of the proposed slot-liner confined EC, a 72 slot 12 pole 125 kW three-phase jacket cooled BMW i3 motor has been chosen as base configuration [20], as shown in Fig. 2. Two-layers of magnet have been buried in rotor lamination, sliced into six axial segments, and stacked in a skewed arrangement to reduce the torque ripple, cogging torque, and magnet loss [21]. Shrink fitted spiral cooling channels have been used to extract heat from the outer surface of the stator lamination. Detailed specification of the BMW i3 motor have been listed in the Table 1.

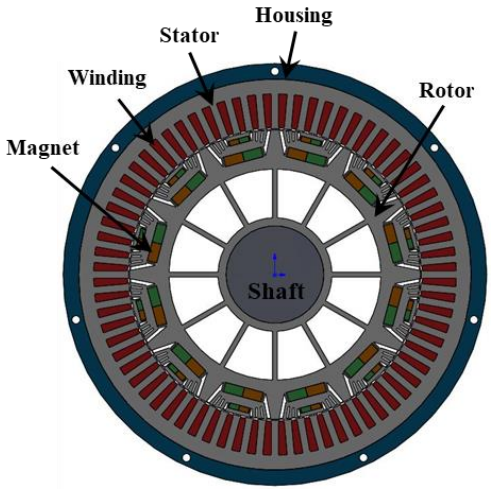

Figure 2: Front view of the BMW i3 motor.

Table 1: BMW i3 motor specifications

Parameters (unit)	Value
Peak/rated torque (N.m)	250/150
Peak/rated power (kW)	125/75
Maximum/rated speed (rpm)	11,400/4,800
DC-link voltage (V)	352
Geometric Specifications	
Stator OD (mm)	240.9
Stator ID (mm)	179.6
Air gap (mm)	0.5
Active length (mm)	130
Total length (mm)	222
Stator/rotor lamination	M250-35A
Magnet	N42UH
Impregnation material	Varnish
Liner material	CeQUIN I
Liner thickness (mm)	0.3
Liner conductivity (W/m.K)	0.195
Weight (kg)	39.39
Volume (L)	11.79
Winding configuration	
Number of turns per coil	9
Number of strands in hand	12
Parallel path	6
Total number of wire	108
Copper slot fill factor	0.3332
Motor cooling	
Housing material	Aluminum (Al)
Housing diameter (mm)	260
Coolant	ethylene-glycol 50/50

For EC, the same motor topology of BMW i3 has been used, with the exception that the spiral cooling channel has been removed, and CeQUIN I liner has been replaced with a 0.3 mm thick PDMS liner (with a thermal conductivity of 0.15 W/m.K [22]), modified with wick structure. Since in the case of EC, the coolant will be in direct contact with the winding, it needs to be dielectric to ensure electrical integrity of the winding. After considering dielectric strength, boiling temperature, vapor pressure, and thermal conductivity requirement, dielectric coolant FC-84 with a saturation temperature of 80°C has been chosen for the EC simulation [23]. Since in the case of EC, coolant will flow through the liner, a thinner (taken as 2 mm in this study) Al casing can be used to protect the motor core from the ambient. For the same winding configuration, total weight and volume of the evaporative cooled BMW i3 motor are estimated as 36.49 kg and 10.45 L, respectively, which are 7.4% and 11.4% less compared to the state-of-the-art jacket cooled BMW i3 motor. It is worth mentioning that for the same output power as BMW i3 motor, improved thermal performance of EC will allow further shrinkage of the motor size by permitting higher current density.

IV. Numerical Modeling

A. Electro-magnetic Simulation

A Finite element model has been built in Motor-CAD to assess the EM performance of both cooling configurations. In order to reduce the computational cost, a single rotor pole and the corresponding stator configuration have been considered as computational domain for the EM simulation, as shown in the Fig. 3. Al housing and cooling channels were not included in the simulation domain.

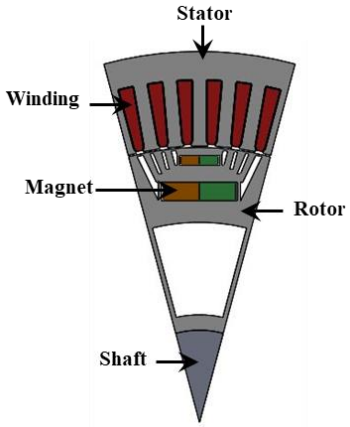

Figure 3: Computational domain of 2D electro-magnetic simulation.

EM torque, Tr_e has been calculated as follows [24]:

$$Tr_e = \frac{m}{2} p\left(\lambda_d I_q - \lambda_q I_d\right) \quad (1)$$

Where m is the number phase, P is the number of pole pairs, λ_d and λ_q are d and q-axis flux linkage, and I_d and I_q are d and q-axis current, respectively. λ_d depends on the residual magnetic flux density, B_{res} which has been calculated using the following equation [25]:

$$B_{res} = B_{res,ref(20)}\left(1 + \frac{\alpha\left(T_m - T_{ref.temp(20)}\right)}{100}\right) \quad (2)$$

This article has been accepted for publication in a future issue of this journal, but has not been fully edited. Content may change prior to final publication. Citation information: DOI 10.1109/TTE.2021.3107505, IEEE Transactions on Transportation Electrification

Where, T_m is the magnet temperature, $B_{res,ref(20)} = 1.31T$ at reference temperature of 20 °C and the temperature coefficient (α) is -0.12/°C [26].

Shaft torque (Tr_s) has been calculated as follows:

$$Tr_s = Tr_e - \left[\left(P_{core} + P_{mag}\right)/\omega\right] \quad (3)$$

Where, ω is the shaft speed, P_{core} and P_m are core and magnet losses, respectively.

P_{core} has been calculated using the modified Steinmetz iron loss model [25]:

$$P_{core}\left(W/_{kg}\right) = K_h f.B^{\gamma+\vartheta B} + 2\pi^2 K_{eddy} f^2 B^2 \quad (4)$$

Where, K_h, γ, ϑ and K_{eddy} have been determined using curve fitting techniques in Motor-CAD.

P_{mag} has been calculated by knowing magnet eddy current from diffusion equation [25].

Copper loss/DC loss in the active and end-winding, and AC loss in the active-winding have been calculated by using the following equations [25]:

$$P_{DC} = 3I^2 R_a[1 + a_T(T_w - T_a)] \quad (5)$$

$$P_{AC} = \frac{\pi D^2(\omega B)^2}{128R_a[1+a_T(T_w-T_a)]} \quad (6)$$

Where, R_a is the electrical resistivity at ambient temperature (T_a) of 20°C, T_w is the copper wire temperature, and D is the wire diameter.

The overall efficiency has been calculated as follows:

$$\eta = \frac{P_{out}}{P_{out}+P_{DC}+P_{AC}+P_{core}+P_{mag}} \quad (7)$$

Where, $P_{out} = (Tr_s\omega)$ is the output power.

Moreover, mechanical and windage losses have been neglected in the EM simulations.

B. Heat Transfer Modeling for JC

Lumped Parameter Thermal Network (LPTN) Model

To accurately and efficiently compute heat transfer in radial and axial directions, a 3D LPTN model including the JC circuit has been developed based on the jacket cooled BMW i3 motor geometry in the Motor-CAD environment. Figure 4 presents the adopted axial thermal network layout where black, blue, and white lines indicate conduction, natural convection to the end-space, and forced convection in outer jacket, respectively. Additionally, in order to assess the axial heat transfer, motor has been split into three longitudinal slices. The active and end-winding regions use cuboidal element approach as explained in [27], where the winding compounds are modeled as a single component with anisotropic thermal conductivity which will be discussed in the forthcoming section. The active and end-winding regions use four radially distributed cuboidal elements, and stator tooth region is also modeled accordingly (see Fig. 4 and 5).

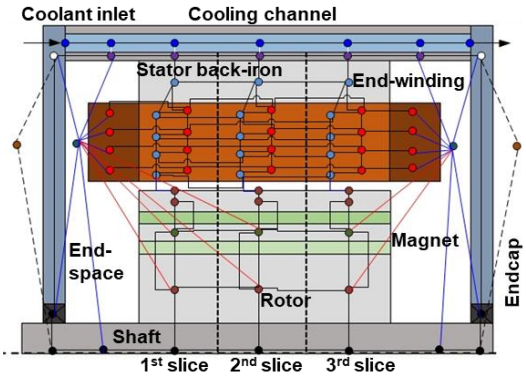

Figure 4: 3D LPTN model layout.

Figure 5 shows radially discretized winding region along with four cuboids, where blue and red resistances indicate winding-liner and liner-lamination contact resistances, respectively. It is worth underlining that skewed cuboidal model has been utilized to accurately capture AC loss [25], especially in the slot opening region, and contact resistances are calculated using individual cuboid dimensions.

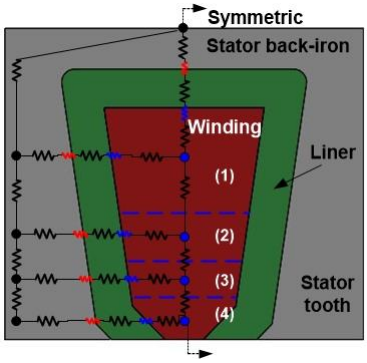

Figure 5: Schematic of the resistance network of single slot, liner, and the corresponding stator lamination (schematic not drawn to scale). Blue and red resistances indicate winding-liner and liner-lamination contact resistances, respectively.

High rotational speed of rotor creates regular air vortex pattern inside the air gap and increase the heat transfer between stator and rotor. Heat transfer across-the air gap has been calculated based on correlations proposed by Taylor [25]:

$$Ta = \frac{l_{air\ gap}\omega r_r}{\vartheta\left(l_{air\ gap}/r_r\right)^{0.5}} \quad (8)$$

$$\begin{aligned} Nu &= 2 && (Ta < 41) \\ Nu &= 0.212Ta^{0.63}Pr^{0.27} && (41 \le Ta \le 100) \\ Nu &= 0.386Ta^{0.5}Pr^{0.27} && (Ta > 100) \end{aligned} \quad (9)$$

$$h = \frac{Nuk_{air}}{2l_{air\ gap}} \quad (10)$$

Where, Ta is the Taylor number, $l_{air\ gap}$ is the air gap length, ω is the rotational speed, r_r is the rotor radius, ϑ is the kinematic viscosity, Pr is the Prandtl number, k_{air} is the air gap thermal conductivity, Nu is the Nusselt number, h is the heat transfer coefficient. Air properties have been calculated as a function of temperature.

Considering fully developed turbulent flow, forced convective heat transfer has been calculated using the Gnielinski correlations [25]:

This article has been accepted for publication in a future issue of this journal, but has not been fully edited. Content may change prior to final publication. Citation information: DOI 10.1109/TTE.2021.3107505, IEEE Transactions on Transportation Electrification

$$v = Q/A;\ Re = \frac{vD_h}{\vartheta} \quad (11)$$

$$f = (0.79 \ln Re - 1.64)^{-2} \quad (12)$$

$$Nu = \frac{(f/8)(Re - 1000)Pr}{[1 + \{12.7(f/8)^{0.5}(Pr^{2/3} - 1)\}]} \quad (13)$$

$$h = \frac{Nuk_l}{D_h} \quad (14)$$

Where, Q is the flow rate, v is the velocity, A is the cross-sectional area, D_h is the hydraulic dimeter, Re is the Reynold's number, f is the friction factor, and k_l is the coolant thermal conductivity.

Heat transfer from the rotor, magnet, and the end-winding to the end-spaces have been calculated as in [25]. Heat will be transferred from the rotor slots to the end-spaces via forced convection. Considering high rotational speed and the complicated rotor duct geometry (see Fig. 2), a constant forced convective heat transfer coefficient of 150 W/m^2.K has been chosen. Brown lines in Fig. 4 indicate heat transfer from the rotor slots to the end-spaces. Additionally, natural convection heat transfer from the housing to the ambient and all radiation heat transfer have been neglected in the LPTN model. Calculated power losses from the EM simulation have been applied as heat sources. For transient simulations, components thermal capacities have been added in the LPTN model.

Computational Fluid Dynamics/Heat Transfer (CFD/HT) Model

Figure 6 illustrates the computational domain for the CFD/HT simulations. In order to reduce the computational cost, only 1/12th of the cross-section, consisting of one rotor pole and the corresponding stator core, six windings and liners, air gap, and housing, has been chosen as computational domain by realizing angular symmetry (see Fig. 6). Additionally, 1/6th axial section of the total active length has been modeled, assuming negligible temperature change along the axial direction, i.e., axial symmetry.

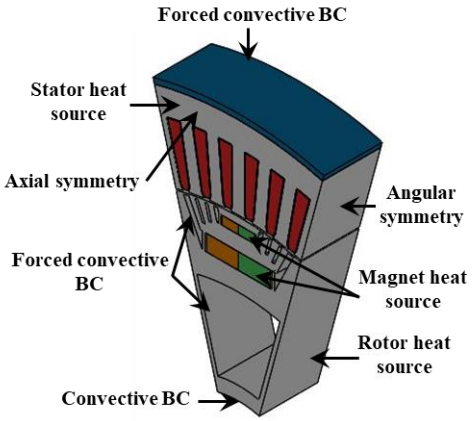

Figure 6: Computation domain and boundary conditions for CFD/HT simulation of JC.

Assuming negligible radiation heat transfer, uniform distribution of heat sources, isotropic thermal conductivity (k) for magnet, liner, and housing materials, and anisotropic k for winding and lamination materials, 3D heat conduction equation has been solved:

$$\frac{1}{r}\frac{\partial}{\partial r}\left(k_r r \frac{\partial T}{\partial r}\right) + \frac{1}{r^2}\frac{\partial}{\partial \theta}\left(k_\theta r \frac{\partial T}{\partial \theta}\right) + \frac{\partial}{\partial z}\left(k_z \frac{\partial T}{\partial z}\right) + q''' = \rho C_p \frac{\partial T}{\partial t} \quad (15)$$

Where, q''' is the volumetric heat generation rate calculated from the EM model, ρ is the density, C_p is the specific heat. In case of steady-state simulation, right hand side Eq. (15) has been neglected.

JC has been simulated as a forced convection boundary condition (BC) on the housing surface:

$$-k\frac{\partial T}{\partial r} = h(T_{sur} - T_f) \quad (16)$$

Where, h is calculated from Gnielinski correlations (see Eq. 11-14), T_{sur} is the average surface temperature, and T_f is the coolant temperature. Since cooling channel has not been considered in the CFD/HT model, T_f has been imported from the LPTN model. Similarly, heat transfer from rotor ducts has been modeled as convection BC with a heat transfer coefficient of 150 W/m^2.K (see Fig. 6), as explained earlier. Additionally, a convective BC is also applied on the rotor bottom face to model heat transfer via shaft.

After a sequential mesh independent testing, 1.9 million of mesh has been used for the CFD/HT simulations. 3D CFD/HT simulations performed in finite volume based software ANSYS Fluent®. Energy equation has been discretized using second order upwind scheme and solution has been assumed to be converged when the residuals reduced below 10^{-9}.

C. Modeling of Evaporative Heat Transfer

LPTN Model

In the case of EC, coolant flows between the active-winding and liner, and evaporates directly on the outer surface of the active-winding by absorbing heat from the winding. Therefore, in the LPTN model, winding-liner contact resistance has been neglected as illustrated in the Fig. 7. Moreover, in the case of thin-film evaporation, coolant temperature can be assumed as constant at saturation temperature. To simplify the evaporation model, winding-liner interface nodes (orange nodes in the Fig. 7) have been connected with constant

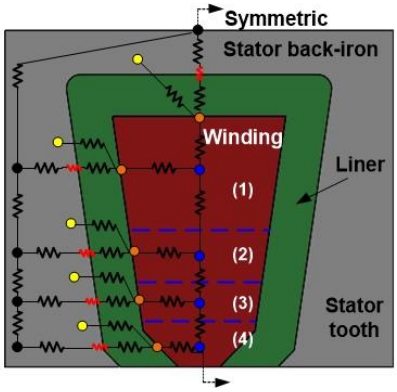

Figure 7: Schematic of resistance network of single slot, liner, and the corresponding stator lamination for EC (schematic not drawn to scale). Red resistance indicate liner-lamination contact resistance and yellow nodes are set at constant saturation temperature of 80°C.

saturation temperature nodes (yellow nodes) via a convective resistance, $R_{c,eva}$ (see Fig. 7):

$$R_{c,eva} = \frac{1}{h_{eva} A_{int.}} \quad (17)$$

Where, A_{int} is the cuboidal interface area between the winding and liner, and has been calculated for individual cuboids, h_{eva} is the evaporative heat transfer coefficient which has been assumed to be known. Since in this paper, FC-84 has been chosen as coolant with a saturation temperature of 80 ºC [23], constant temperature nodes (yellow nodes in the Fig. 7) are set at that temperature. Moreover, external JC circuit has been removed from the 3D LPTN model.

CFD/HT Model

In the CFD/HT model, an evaporative heat absorption term as a negative heat source in the liner has been introduced in the energy equation:

$$Q_{eva} = -h_{eva} A_{int.} \left(T_{wind,o} - T_{sat}\right) \quad (18)$$

Where, Q_{eva} is the overall heat absorption via evaporation, A_{int} is the interfacial area of the winding and the liner, $T_{wind,o}$ is the average winding outer surface temperature. Since, Q_{eva} depends on the instantaneous winding temperature, negative heat source term in the CFD/HT simulation has been implemented via a User Defined Function (UDF) in ANSYS Fluent®.

D. Electro-magnetic and HT Simulation Coupling

It is worth recalling that EM and thermal performances of the electric motor are strongly dependent on each other via winding and magnet temperatures, and power losses. Therefore, EM and thermal simulations have been performed in a two-way coupled environment. Detailed flowchart of the coupled EM and heat transfer modeling is presented in Fig. 8 and can also be found in [4]. In the forthcoming sections, coupled EM-CFD/HT and EM-LPTN simulations have been abbreviated as only CFD and LPTN, respectively.

E. Contact Resistance

Thermal contact resistance $(R_{t,c})$ between rotor lamination-magnet, winding-slot liner, slot liner-stator lamination, and stator lamination-housing (for JC) have been shown to have significant effect on the motor temperature distribution. Table 2 summarizes equivalent air gap cavity thicknesses (l_g) and the corresponding thermal contact conductances. To the best of the authors' knowledge, winding-liner, and liner-stator lamination $R_{t,c}$ data for BMW i3 motor are not available in the literature. However, Wrobel et al. [28] calculated equivalent winding-stator lamination l_g of 0.06 mm for CeQUIN I liner material (which is typically used in BMW i3 motor). Additionally, NREL reported that winding-liner $R_{t,c}$ is about 3 times higher than liner-stator $R_{t,c}$ for Nissan Leaf motor [19]. By combining Wrobel et al. and NREL's finding and assuming similar winding-liner $R_{t,c}$ for BMW i3 as Nissan Leaf motor, l_g between winding-liner and liner-lamination, and the corresponding conductance's have been calculated, as shown in the Table 2.

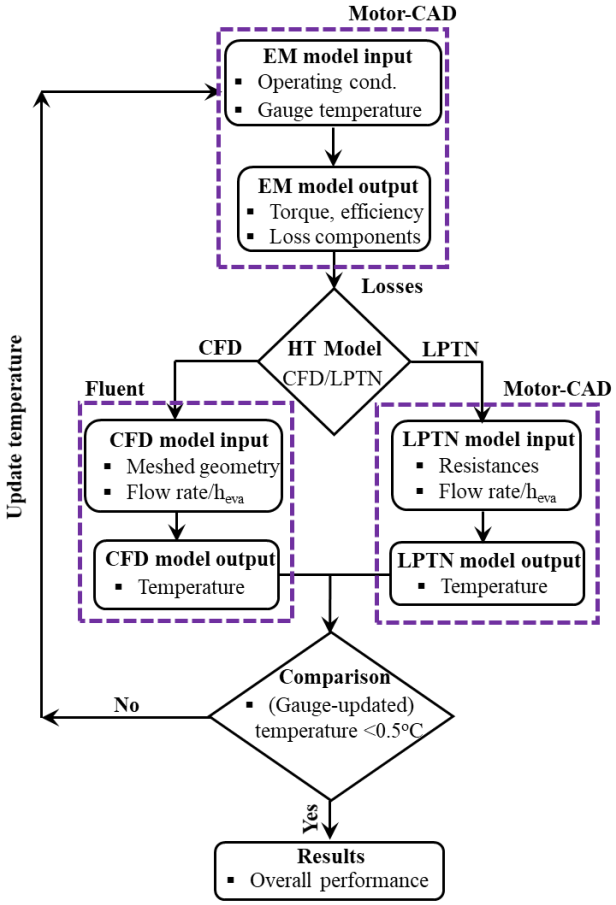

Figure 8: Two-way coupling algorithm.

Table 2: Equivalent air gap cavity thickness and conductance for JC

Interface	Equivalent air gap thickness (mm)	Conductance[1] (W/m².K)
Rotor lamination - magnet	0.005	6,342
Stator lamination - housing	0.0057	5,563
Winding - liner	0.045	705
Liner – stator lamination	0.015	2,114

[1]For conductance calculation, air thermal conductivity has been assumed as constant 0.03171 W/m².K.

The same $R_{t,c}$ have also been used for EC, except winding-liner $R_{t,c}$. As explained earlier, in case of EC, the coolant is in direct contact with the winding, therefore, winding-liner $R_{t,c}$ has been neglected. In the LPTN model, all $R_{t,c}$ have been inputted directly and in the CFD model, equivalent l_g has be used to model $R_{t,c}$.

F. Thermo-physical Properties of Winding and Lamination

Winding is a heterogeneous mixture of copper wire, wire insulation, and impregnation materials. In order to model it as a single material, equivalent radial/circumferential thermal conductivity (k_r/k_θ) has been calculated from the relative volume of the copper wire (slot fill factor), impregnation (considering goodness factor (GF)), and insulation materials as

This article has been accepted for publication in a future issue of this journal, but has not been fully edited. Content may change prior to final publication. Citation information: DOI 10.1109/TTE.2021.3107505, IEEE Transactions on Transportation Electrification

Table 3: Properties of winding and lamination materials

Component	Winding			Lamination	
Material	Cu	Insulation	Impregnation	M250-35A	Inter-lamination
k (W/m.K)	401	0.21	0.25	30	0.027
ρ (kg/m^3)	8933	1400	1400	7650	1127
C_p (J/kg.K)	385	1000	1700	460	1007
Fill/packing factor		0.3332		0.97	
Equivalent $k_r/k_\theta/k_z$		0.50/0.50/166		29.1/29.1/1.13	
Equivalent ρ		4366.98		7420.53	
Equivalent C_p		564.11		460	

described in [29]. Winding axial thermal conductivity (k_z), equivalent density (ρ), and specific heat (C_p) have been calculated using the parallel model as shown in [29].

Similarly, equivalent axial thermal conductivity (k_z), density (ρ), and specific heat (C_p) of the lamination material, considering a packing factor of 0.97, have also been calculated using the parallel model [30]. Table 3 summarize the calculated thermo-physical properties of the winding and lamination.

V. Model Validation

Accuracy and reliability of the developed two-way coupled LPTN and CFD model have been validated by comparing numerically calculated shaft toque under different current loading with the benchmarking testing data of jacket cooled BMW i3 motor reported by Oak Ridge National Laboratory (ORNL) [21]. From Fig. 9, it is evident that the calculated torque from both models shows good agreement with the experimental results. The average deviation between the experimental and LPTN results was less than 3.74%, whereas the average deviation between the experimental and CFD results was less than 3.66%.

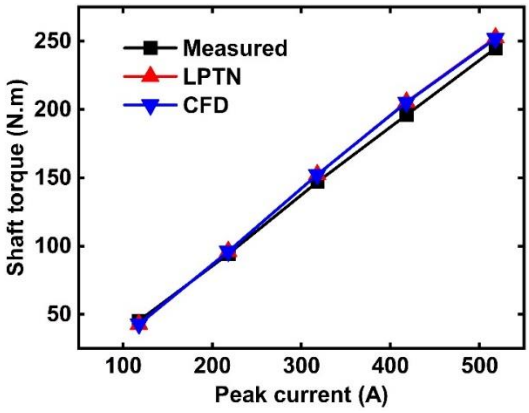

Figure 9: Comparison between experimentally measured shaft torque reported by ORNL [21] and numerically calculated shaft torque from LPTN and CFD models at a coolant flow rate of 10 L/min and coolant inlet temperature of 65°C.

In order to validate the heat transfer model, calculated average end-winding temperature from LPTN model has been compared with the experimentally measured end-winding temperature reported by ORNL over a continuous test at two different power levels of 25 kW and 50 kW, respectively [21]. From Fig. 10 (a), it can be seen that the LPTN model can accurately predict the temporal temperature change of the end-winding for both loading conditions, with a maximum temperature difference less than 1ºC. Since the end-winding section has not been modeled in the CFD model, it has been validated by comparing transient average active-winding and magnet temperatures with the LPTN model as shown in the Fig. 10 (b). The comparison illustrates that both models are in excellent agreement under dynamic loading. At quasi-steady condition, maximum deviation between average active-winding temperature calculated from LPTN and CFD models was 1.22ºC. Similarly, maximum deviation between the average magnet temperature calculated from LPTN and CFD models was 0.68ºC.

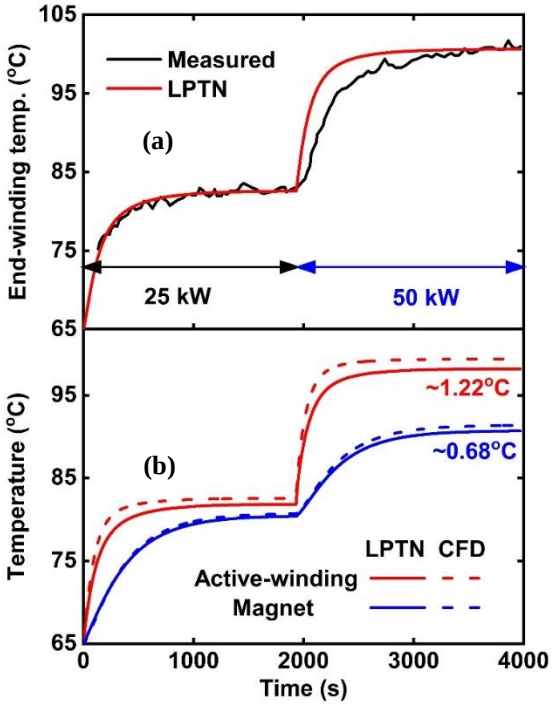

Figure 10: (a) Comparison between measured average end-winding temperature reported by ORNL [21] and numerically obtained end-winding temperature from LPTN model, (b) comparison between calculated average active-winding and magnet temperatures from LPTN and CFD models at 5,000 rpm, coolant flow rate of 10 L/min (corresponding h is 5,054 W/m^2.K), and coolant inlet temperature of 65 °C.

VI. Results and Discussions

This article has been accepted for publication in a future issue of this journal, but has not been fully edited. Content may change prior to final publication. Citation information: DOI 10.1109/TTE.2021.3107505, IEEE Transactions on Transportation Electrification

In case of jacket cooled BMW i3 motor, forced convection heat transfer coefficient (h) beyond 5,000 W/m^2.K has negligible effect on the motor temperature distribution, as reported in [6]. Therefore, in this section, coolant flow rate of 10 L/min (corresponding h is 5,054 W/m^2.K) has been considered for JC.

A. Comparison of Electro-Magnetic Performance of JC and EC

Since EM and thermal performance of the electric motor are strongly dependent on each other, EM performance of the proposed EC integrated motor has been compared with the EM performance of JC to justify the overall effectiveness of the proposed EC method. Fig. 11 (a) illustrates the magnetic flux density and flux line distribution for JC and EC. Since slot-liner confined EC does not change winding configurations or slot copper fill factor compared to the JC, flux distribution for EC and JC are very similar (see Fig. 11 (a)). Consequently, EC provides very similar output torque as JC as shown in the Fig. 11 (b). Moreover, at high current density, EC provides slightly higher torque compared to the JC. This gain can be attributed to the thermal benefit of the EC over JC, which will be discussed in detail in the next section.

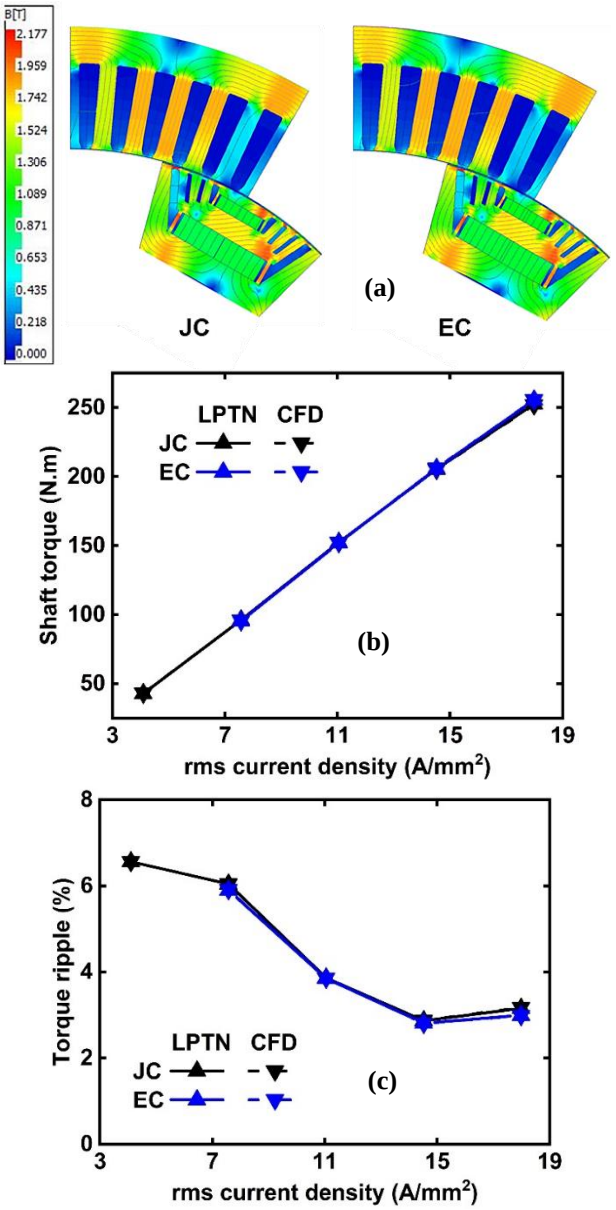

Figure 11: (a) Flux density distribution, (b) shaft torque, and (c) torque ripple vs. rms current density for JC and EC at constant shaft speed of 4500 rpm and phase advance of 45 EDeg. In case of JC, coolant flow rate was 10 L/min (corresponding h was 5,054 W/m^2.K), whereas in case of EC, h_{eva} was 5,000 W/m^2.K. Lowest current density of 4.10 A/mm^2 has not been considered for EC.

Torque quality, i.e., torque ripple of EC has also been compared with JC, as shown in Fig. 11 (b). At lower current density, EC provides similar torque ripple as JC, whereas at higher current density, EC reduces the torque ripple up to ~5.30% compared to the JC.

B. Comparison of Thermal Performance of JC and EC

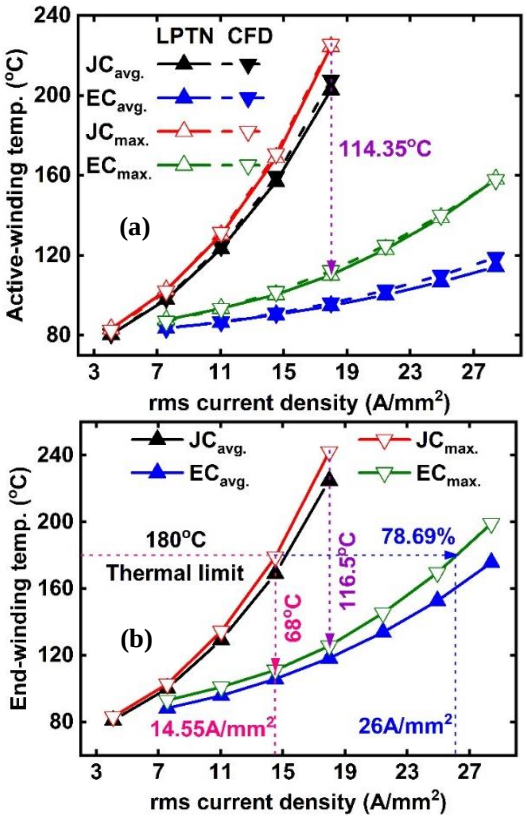

Figure 12: Steady-state (a) active-winding and (b) end-winding temperature vs. rms current density for JC and EC at constant shaft speed of 4500 rpm and phase advance of 45 EDeg. In case of JC, coolant flow rate was 10 L/min (corresponding h was 5,054 W/m^2.K), whereas in case of EC, h_{eva} was 5,000 W/m^2.K. Lowest current density of 4.10 A/mm^2 has not been considered for EC and the end-winding temperature has been calculated from the LPTN model only.

For JC and EC, Fig. 12 (a) depicts steady-state average and maximum active-winding temperature variation with rms current density calculated from LPTN and CFD models. From the figure, it can be observed that EC substantially reduces the active-winding temperature compared to the JC, especially at higher current density, which is our main point of interest. For example, at a current density of 18 A/mm^2 (which corresponds to peak torque of 250 N.m of jacket cooled BMW i3 motor), EC reduces the peak active-winding temperature by ~114.35 ^{o}C compared to the JC. This thermal benefit can be attributed to

This article has been accepted for publication in a future issue of this journal, but has not been fully edited. Content may change prior to final publication. Citation information: DOI 10.1109/TTE.2021.3107505, IEEE Transactions on Transportation Electrification

the overall reduced thermal resistance between the winding and coolant, which is partially due to the elimination of the winding-liner contact resistance for EC. On the contrary, at lower current density, EC marginally reduces the winding temperature because of lower heat losses and relatively higher saturation temperature of the coolant (80 ^{o}C). In case of EC, reduced winding temperature permits higher current density input within the thermal limit of the coil insulation (see Fig. 12 (a)). However, maximum current density is often limited by the peak end-winding temperature, which will be discussed in the next section. Moreover, the predictions of active-winding temperatures by LPTN and CFD models are in excellent agreement, with a maximum difference up to 4.52 ^{o}C.

In the absence of potting material or advanced end-winding cooling and due to the relatively high end-winding length of BMW i3 motor (32 mm), end-winding section exhibits higher temperature compared to the active-winding section and eventually, hotspot appears in the end-winding. Figure 12 (b) compares the average and peak end-winding temperature for EC and JC. As mentioned earlier, the end-section has not been included in the CFD model, therefore, end-winding temperature has been calculated from the LPTN model only. As shown in Fig. 12 (b), EC significantly reduces the end-winding section temperature compared with JC, and this temperature reduction increases with current density. For example, at a current density of 18 A/mm^2, EC reduces the peak winding temperature by more than 116 ^{o}C compared to the JC. Moreover, peak end-winding temperature of the jacket cooled motor reaches the thermal threshold limit of 180 ^{o}C (considering class H insulation) at a current density of 14.55 A/mm^2 (see Fig. 12 (b)). By employing EC, end-winding temperature can be reduced by ~68 ^{o}C at the threshold JC current density of 14.55A/mm^2, allowing more current supply in the winding before reaching the insulation's thermal limit. As illustrated in the Fig. 12 (b), EC can push the current density limit as high as 26 A/mm^2, which is 78.69% higher compared to the JC.

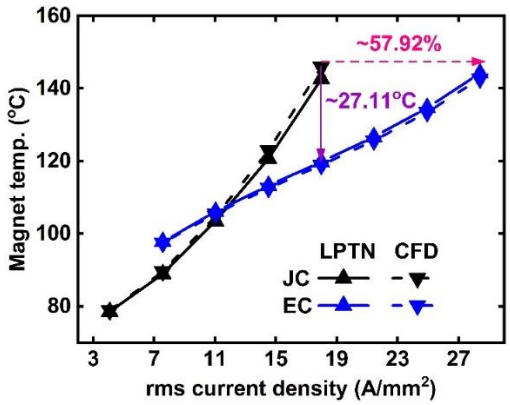

Figure 13: Steady-state magnet temperature vs. rms current density for JC and EC at constant shaft speed of 4500 rpm and phase advance of 45 EDeg. In case of JC, coolant flow rate was 10 L/min (corresponding h was 5,054 W/m^2.K), whereas in case of EC, h_{eva} was 5,000 W/m^2.K. Lowest current density of 4.10 A/mm^2 has not been considered for EC.

Magnet temperature is another critical point of interest for PMSM. High magnet temperature results in lower residual magnetic flux density (see Eq. 2) and premature demagnetization of the magnet. Moreover, air-gap between the stator and rotor often limit the heat exchange between the cooling medium of stator and magnet by imposing high thermal resistance. As shown in the Fig. 13, EC notably reduces the magnet temperature compared to the JC, especially at high current density. For example, at a current density of 18 A/mm^2, EC reduces the magnet temperature by ~ 27^{o}C compared to the magnet temperature of 145 ^{o}C in the case of JC. Furthermore, in the case of EC, current density can be increased up to 28.41 A/mm^2 (about 57.92% increment) for this magnet temperature of 145 ^{o}C (see Fig. 13).

Figure 14 presents the temperature distributions of the motor in the middle plane of the computational domain for JC and EC, respectively. In case of JC, maximum temperature occurs in the winding as expected, and stator back iron exhibits significantly lower temperature compared to the stator tooth. Moreover, high winding-liner, liner-lamination, and lamination-housing contact resistances results in sharp temperature drops across the winding-tooth/back iron and lamination-housing interfaces (see Fig. 14 (a)). In contrast, EC significantly reduces the winding temperature compared to the JC and maintains more uniform temperature throughout the stator tooth and back iron. It is worth noting that EC reduces the temperature drop across the liner by eliminating the winding-liner contact resistance, especially in the winding-stator tooth section. Additionally, in the case of EC, negligible temperature drop is evident across the lamination-housing interface (see Fig. 14 (b) and for both cooling configurations, rotor and magnet assembly show uniform temperature distribution (see Fig. 14).

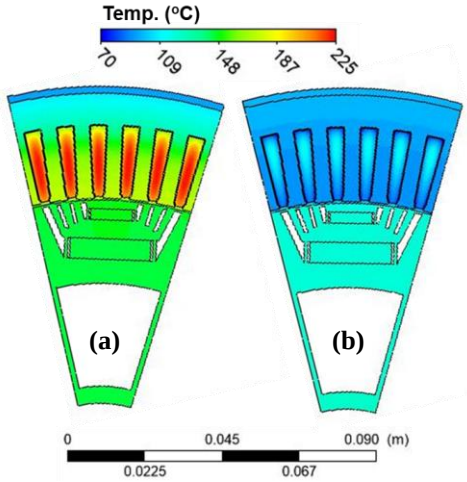

Figure 14: Temperature contour of (a) JC and (b) EC at rms current density of 18 A/mm^2, constant shaft speed of 4500 rpm, and phase advance of 45 EDeg. In case of JC, coolant flow rate was 10 L/min (corresponding h was 5,054 W/m^2.K), whereas in case of EC, h_{eva} was 5,000 W/m^2.K.

C. Comparison of Electro-thermal Performance of JC and EC

Fig. 15 compares copper/DC and AC losses between JC and EC for different current loading. It is worth noting that the copper loss changes nearly linearly with the winding resistance/temperature (see Eq. 5), therefore, copper loss can be reduced by lowering the winding temperature. In contrast, AC loss changes in inverse proportion with the winding temperature (see Eq. 6). In case of EC, lower winding temperature (see Fig. 12) results in lower copper loss and higher AC loss compared to the JC, as shown in Fig. 15. For example,

This article has been accepted for publication in a future issue of this journal, but has not been fully edited. Content may change prior to final publication. Citation information: DOI 10.1109/TTE.2021.3107505, IEEE Transactions on Transportation Electrification

at a current density of 18 A/mm^2, EC reduces the copper loss by 1.1 kW (about 24% reduction) and increases the AC loss by 0.22 kW compared to the JC. Moreover, both LPTN and CFD model's prediction are in close agreement with each other at any particular current density.

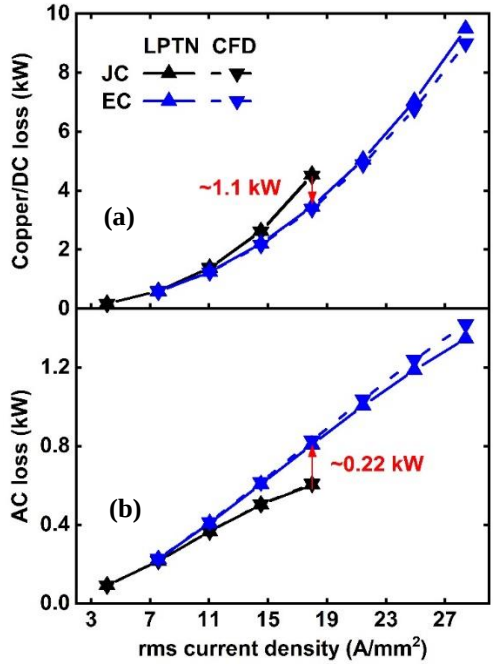

Figure 15: (a) Copper/DC loss and (b) AC loss vs. rms current density for JC and EC at constant shaft speed of 4500 rpm and phase advance of 45 EDeg. In case of JC, coolant flow rate was 10 L/min (corresponding h was 5,054 W/m^2.K), whereas in case of EC, h_{eva} was 5,000 W/m^2.K. Current density of 18 A/mm^2 corresponds to peak operating condition for JC. Lowest current density of 4.10 A/mm^2 has not been considered for EC.

Despite the opposing nature of DC and AC losses, EC reduces the total loss compared to the JC, due to the dominant share of the DC loss, and constant core and magnet losses for both cooling configurations, as shown in the Fig. 16. At the current density of 18 A/mm^2, EC reduces the total loss by 0.88 kW (about 11.70% reduction) compared to the JC.

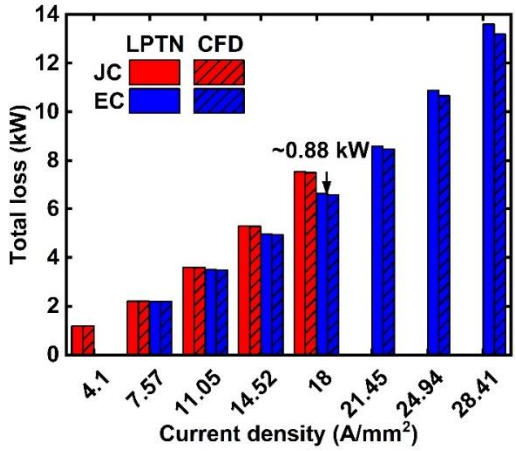

Figure 16: Total loss vs. rms current density for JC and EC at constant shaft speed of 4,500 rpm and phase advance of 45 EDeg. In case of JC, coolant flow rate was 10 L/min (corresponding h was 5,054 W/m^2.K), whereas in case of EC, h_{eva} was 5,000 W/m^2.K. Current density of 18 A/mm^2 corresponds to peak operating condition for JC. Lowest current density of 4.10 A/mm^2 has not been considered for EC.

In case of EC, lower power losses enable higher EM efficiency compared to the JC and this tendency increases with current density. Figure 17 shows that at a current density of 18 A/mm^2, EC offers 0.77% higher electro-magnetic efficiency over the JC. Moreover, at the peak allowable current density of 26 A/mm^2 within the thermal limit (see Fig. 12 (b)), EC can maintain the overall EM efficiency as high as 93.4%.

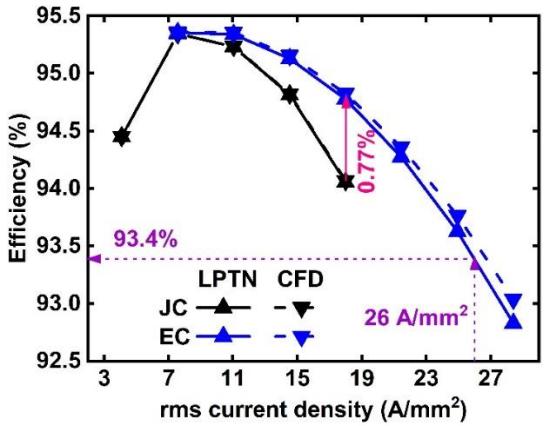

Figure 17: Electro-magnetic efficiency variation as a function of rms current density at constant shaft speed of 4500 rpm and phase advance of 45 EDeg. In case of JC, coolant flow rate was 10 L/min (corresponding h was 5,054 W/m^2.K), whereas in case of EC, h_{eva} was 5,000 W/m^2.K. Current density of 18 A/mm^2 corresponds to peak operating condition for JC. Lowest current density of 4.10 A/mm^2 has not been considered for EC.

D. Transient Thermal Performance

Figure 18 shows transient temperature rise of magnet, active and end-winding temperatures for JC and EC, respectively. From the figure, it can be observed that for both cooling configurations, temporal rise of active-winding and magnet temperatures predicted by LPTN and CFD models are in close agreement throughout the time span considered. It is worth noting that no tuning/correction factor of material properties or geometry has been used to match LPTN and CFD models result. In the case of EC, active and end-winding temperatures reache the quasi steady-state much faster compared to the JC. For example, in case of JC, winding temperature reaches steady-state at around 630 s, whereas in case of EC, winding temperature reaches the quasi steady-state after 210 s of operation. Having the EC in close proximity to the winding substantially reduces the thermal time constant and hence, accelerates the thermal response, compared to the JC. On the contrary, high thermal resistance between the winding and jacket coolant results in larger thermal time constant, and consequently slows down the thermal response for JC.

E. Effect of Evaporative Heat Transfer Coefficient

As reported in [20], h_{eva} can be achieved in the range of 2,000-9,000 W/m^2.K from capillary assisted thin-film evaporation in PDMS microchannel. Since PDMS modified with wick structure has been considered for slot-liner confined EC, effect of h_{eva} on the winding temperature has

This article has been accepted for publication in a future issue of this journal, but has not been fully edited. Content may change prior to final publication. Citation information: DOI 10.1109/TTE.2021.3107505, IEEE Transactions on Transportation Electrification

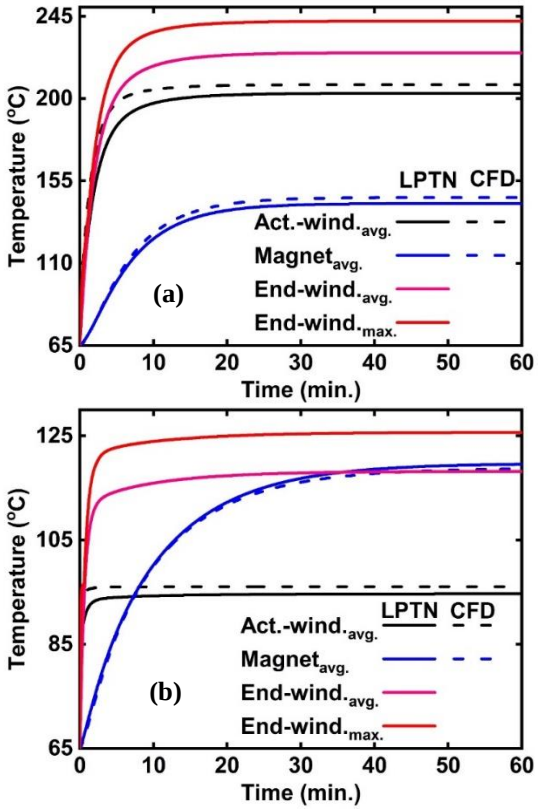

Figure 18: Temporal evaluation of temperature for (a) JC, and (b) EC at constant current density of 18 A/mm^2 (which corresponds to peak operating condition for JC), initial temperature of 65°C, shaft speed of 4500 rpm, and phase advance of 45 EDeg. In case of JC, coolant flow rate was 10 L/min (corresponding h was 5,054 W/m^2.K), whereas in case of EC, h_{eva} was 5,000 W/m^2.K.

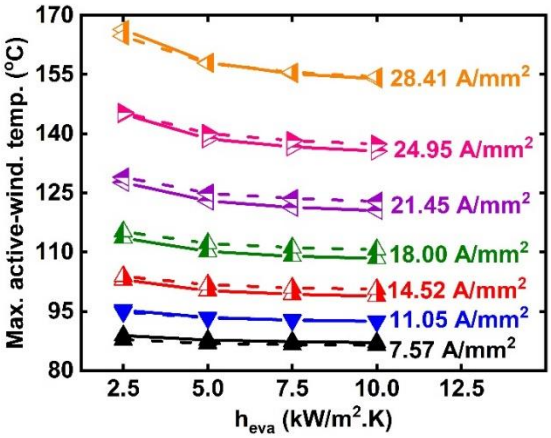

Figure 19: Maximum active winding temperature vs. evaporative heat transfer coefficient at a constant shaft speed of 4500 rpm, and phase advance of 45 EDeg. The solid lines indicate results by LPTN model and the dashed line indicate results by the CFD model.

has been examined over a wide range of h_{eva}, from 2,500-10,000 W/m^2.K. From the Fig. 19, it can be seen that at any particular current density, h_{eva} has negligible effect on the winding temperature above a threshold limit of 5,000 W/m^2.k, indicating insensitive convective resistance between the winding-cooling medium above the threshold h_{eva}. For example, at the highest current density of 28.41 A/mm^2, maximum active-winding temperature reduced by only ~4°C for a h_{eva} increment from 5,000 to 10,000 W/m^2.K.

F. Enhancement of Evaporative Cooling

Complex heterogeneous nature of windings results in poor equivalent thermal conductivity, especially in radial and tangential directions. In the case of EC, lower winding thermal conductivity imposes high conduction resistance between the winding and coolant and eventually, hinders heat extraction from the winding, even at high h_{eva} (see Fig. 19). Conduction resistance between the winding and the coolant can be reduced by increasing winding thermal conductivity, and in turn, enhanced effectiveness of the EC can be realized. For the same copper fill factor and Goodness Factor (GF), winding thermal conductivity can be increased by choosing appropriate impregnation material with high thermal conductivity. LORD CoolTherm® EP-2000 epoxy with a thermal conductivity of 1.9 W/m.K [30] can be used as impregnation material. Moreover, low viscosity of EP (~1.9 Pa.s [31]) ensure similar GF as varnish impregnation. Therefore, for this work, same GF of 0.8 has been considered for both varnish and EP impregnation material. Table 4 summarize thermo-physical properties of the varnish and EP impregnated winding. EP impregnation increases the radial and tangential thermal conductivities by ~ 2.87 times compared to varnish impregnation.

Table 4: Thermo-physical properties of the Varnish and EP impregnated windings

Impregnation material		Varnish	EP
Thermal conductivity (W/m.K)		0.25	1.9
Dielectric strength (kV/mm)		80	18.5
Volumetric resistivity at 25°C (Ω.cm)		10^{15}	10^{14}
Viscosity (Pa.s)		-	1.9
Winding orthotropic thermal conductivity (W/m.K)	k_r	0.5	1.4
	k_θ	0.5	1.4
	k_z	166	166.6

A comparison between the steady-state maximum end-winding (hot spot) temperatures of the JC, EC with varnish impregnation, and EC with EP impregnations (EC_{EP}) at different rms current densities is presented in Fig. 20. As shown, compared to the JC, EC_{EP} substantially reduces the hot spot temperature at any specific current density, and the effectiveness of EC_{EP} gradually increases with current density. These thermal benefits can be attributed to the higher winding thermal conductivity and consequently, lower conduction resistance between the slot center and the coolant. For example, at a current density of 26 A/mm^2 (which is the maximum allowable current density for continuous operation of EC), EC_{EP} reduces the hot spot temperature by 30 °C compared to the EC. Furthermore, in case of EC_{EP}, continuous current density can be increased up to 30 A/mm^2 within the thermal limit of the winding insulation, which is ~15.38% and ~106.19% higher compared to the EC and JC, respectively. It is worth noting that the higher thermal conductivity of the impregnation material can push the current density boundary beyond the limit presented in this paper.

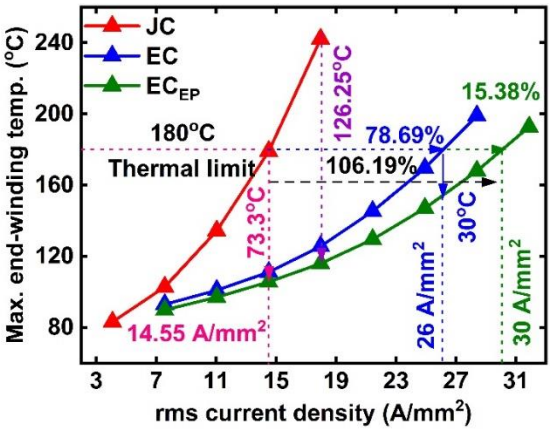

Figure 20: Steady-state maximum end-winding temperature vs. rms current density for JC, EC, and EC$_{EP}$ at constant shaft speed of 4500 rpm and phase advance of 45 EDeg. In case of JC, coolant flow rate was 10 L/min (corresponding h was 5,054 W/m^2.K), whereas in case of EC and EC$_{EP}$, h_{eva} was 5,000 W/m^2.K. Lowest current density of 4.10 A/mm^2 has not been considered for EC.

G. Peak Transient Operating Condition

Figure 22 (a) presents calculated time to reach the thermal limit of the class H insulation as a function of the rms current density for EC$_{EP}$. Since EC$_{EP}$ enables highest steady-state current density (30 A/mm^2) compared to JC and EC (see Fig. 20), for peak transient condition, only EC$_{EP}$ has been chosen and investigated for the transient thermal performance above the current density of 30 A/mm^2. Required time to reach the insulation thermal limit decreases exponentially as current density increases. Similar exponentially decaying nature with time to reach the insulation thermal limit was also reported for DWHX [7]. Since peak load condition is characterized as 30 s load, rms current density of 40.81 A/mm^2 has been extracted as peak electrical loading for EC$_{EP}$ from Fig. 22 (a). Figure 22 (b) shows the temporal temperature change of the magnet, active and end-winding temperature for EC$_{EP}$ and at a current density of 40.81 A/mm^2. As shown, winding hotspot temperature reaches 180 °C after 30 s of operation.

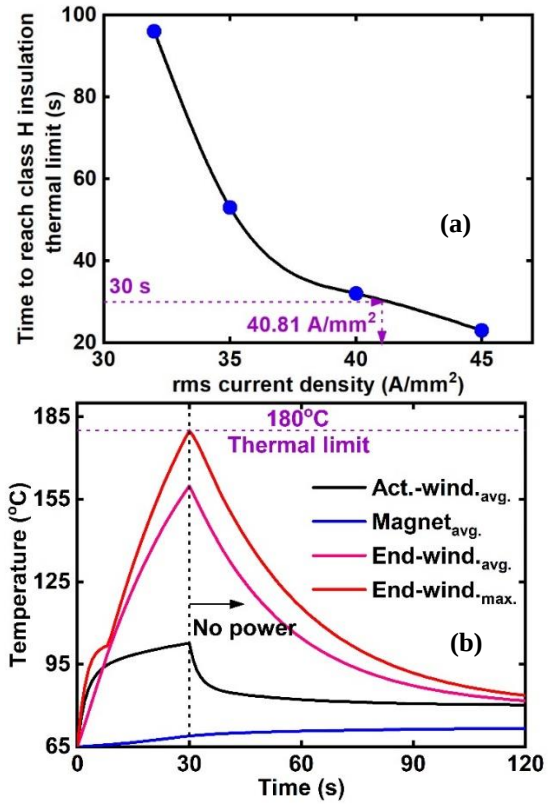

Figure 21: (a) Time to reach class H insulation thermal limit of 180°C vs. rms current density and (b) temporal evaluation of temperature for EC$_{EP}$ at rms current density of 40.81 A/mm^2, initial temperature of 65°C, shaft speed of 4500 rpm, and phase advance of 45 EDeg and h_{eva} of 5,000 W/m^2.K.

H. Thermal Performance Comparison Over Duty Cycle

Dynamic thermal performance of the EC has been compared with JC over a duty cycle at a constant speed of 4,500 rpm. Custom duty cycle has been defined as follows: torque is kept at 60% (150 N.m, which corresponds to rated condition) of the peak torque of the BMW i3 motor, and three 40 s long 250 N.m peak square torque pulses are applied, as shown in Fig. 22. The corresponding winding, core, and magnet losses have been calculated for all cooling configurations. However, the negligible magnet loss has not been plotted in the Fig. 22. As shown, EC and EC$_{EP}$ provide higher winding losses upto 240 s because of the higher AC loss compared to the JC. In contrast, beyond 240 s., EC and EC$_{EP}$ provide lower DC, i.e., winding loss.

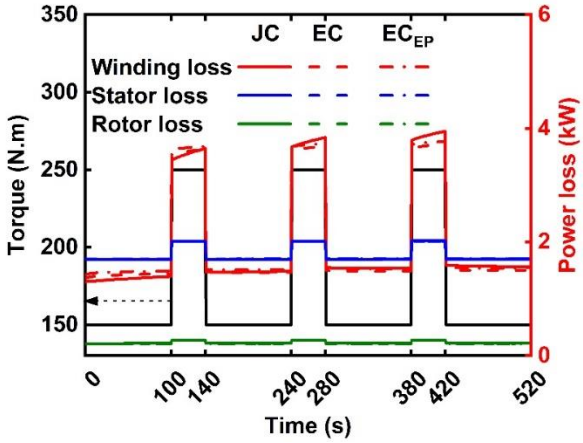

Figure 22: Torque and corresponding power losses vs. time at constant shaft speed of 4500 rpm and phase advance of 45 EDeg. In case of JC, coolant flow rate was 10 L/min (corresponding h was 5,054 W/m^2.K), whereas in case of EC and EC$_{EP}$, h_{eva} was 5,000 W/m^2.K.

Figure 23 compares the temporal change of maximum end-winding (hotspot) and magnet temperatures between JC, EC, and EC$_{EP}$ over the customized drive cycle. In case of JC, hotspot temperature increases gradually with time because of the high thermal time constant. On the other hand, in case of EC and EC$_{EP}$, low thermal time constant results in nearly steady-periodic hotspot temperature change, especially after the first torque pulse at 140 sec. From the figure, it can also be seen that both EC and EC$_{EP}$ substantially reduce the hotspot temperature, particularly after the first torque pulse and this trend is more pronounced after each progressive torque pulse. For example, at ~500 s, EC$_{EP}$ reduces the peak winding temperature by 50 °C. Moreover, EC marginally reduces the magnet temperature (less than 5 °C) compared to the JC, as shown in Fig. 23.

This article has been accepted for publication in a future issue of this journal, but has not been fully edited. Content may change prior to final publication. Citation information: DOI 10.1109/TTE.2021.3107505, IEEE Transactions on Transportation Electrification

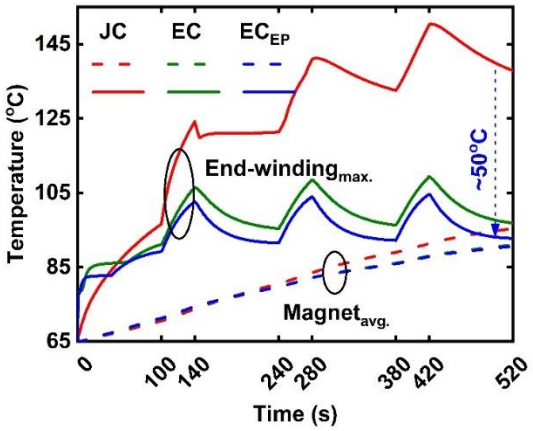

Figure 23: Temporal hot spot and average magnet temperatures change over a dynamic duty scale at constant shaft speed of 4500 rpm and phase advance of 45 EDeg. In case of JC, coolant flow rate was 10 L/min (corresponding h was 5,054 W/m^2.K), whereas in case of EC and EC$_{EP}$, h_{eva} was 5,000 W/m^2.K.

VII. Experimental Validation

A. Motorette Test setup

In order to validate the simulation results presented in the previous sections, a 2 kW DC motorette testbed with 8 slots is designed and fabricated. Although stator of a real motor is made from compressed sheets of laminated steels, but to simply the experiment setup, an aluminum bar was used to fabricate the motorette testbed. The major components of design include three design parts: coolant reservoir, endcap to cover end-windings, and the active part with the slots and wick enhanced PDMS liner (see Fig. 24 (a)). It is worth noting that motorette slot size is identical to BMW i3 motor winding slot and motorette slots were hand-wound with 108 turns AWG 21 enameled magnet copper wire. Figure 24 (b) illustrates a schematic of the coolant flow through the motorette testbed. From the upstream reservoir, the coolant is pumped into the slot liner through the top hole (see Fig. 24 (c)). Afterwards, the

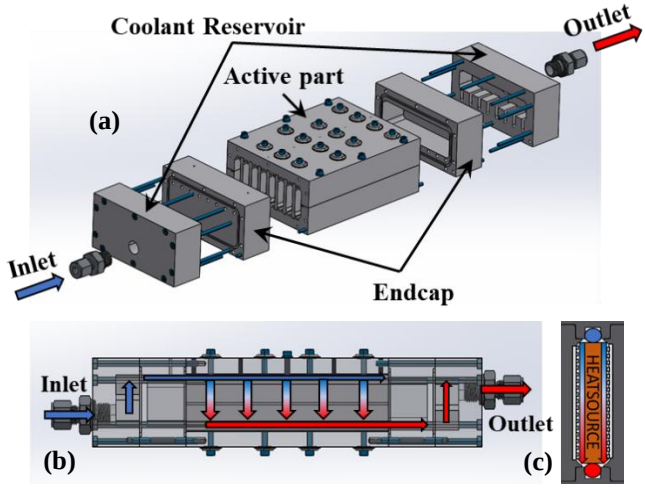

Figure 24: (a) Expanded view of the motorette assembly, (b) schematic of coolant flow path through the testbed, and (c) front view of a single slot.

coolant flows downward, assisted by the capillary action of the wick while evaporating. Finally, the mixture of liquid and vapor (two-phase flow) exits the bottom hole of the slot (see Fig. 24 (c)), and is condensed back to liquid outside of the testbed through the outlet. The winding was powered by Agilent Technologies N8931A DC power supply. Six T-type sheathed probe thermocouples were axially placed inside a single slot to accurately measure the winding temperature profile.

The cooling loop includes a liquid pump, a heat exchanger, accumulator/phase separator (reservoir), flowmeter, data acquisition system, and a DC power source (see Fig. 25). Flow rate, inlet and outlet temperature, and temperature within the testbed were recorded using Agilent 3970A data acquisition system.

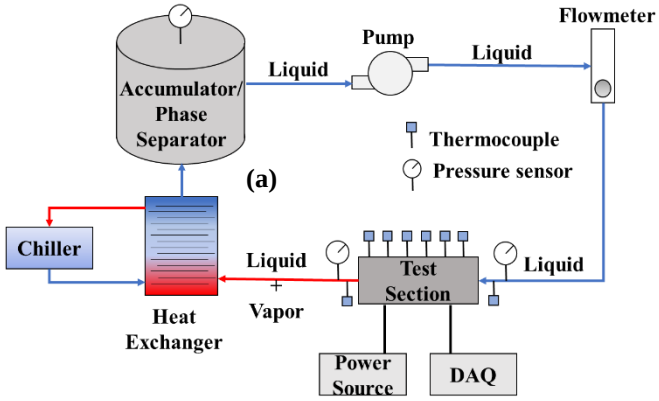

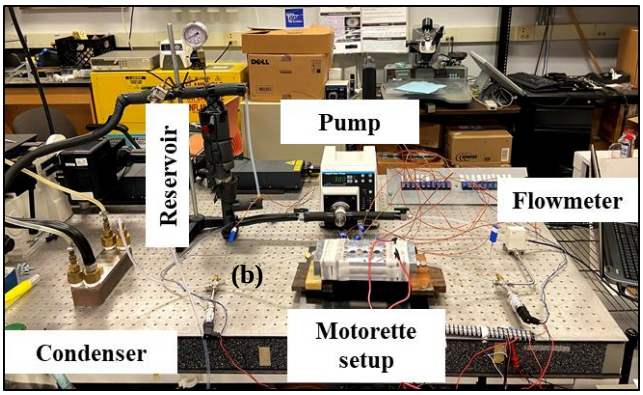

Figure 25: (a) Schematic of the flow loop (b) actual setup with the motorette in the two phase loop.

The motorette testbed was prepared with an intention to test the EC performance inside impregnated slots. However, due to some technical issues of the impregnation curing oven, impregnation material could not be applied in the motorette slot. Therefore, EC testing has been performed in non-impregnated motorette setup. It is worth noting that due to the absence of impregnation material, coolant was not only confined in between the liner and winding, and some coolant may enter inside the slots. Additionally, dielectric coolant Novec-7200 with a saturation temperature of 76°C has been used for the motorette testing.

B. CFD/HT Model

To mimic the motorette testing, a modified CFD/HT model has been developed for the thermal simulation shown in Fig. 26 following a methodology similar to described in Section IV. A single slot has been used for the CFD/HT modeling using symmetric BCs and only active-winding has been considered (see Fig. 26). For EC modeling, modeling approach described in the Section IV has been utilized.

This article has been accepted for publication in a future issue of this journal, but has not been fully edited. Content may change prior to final publication. Citation information: DOI 10.1109/TTE.2021.3107505, IEEE Transactions on Transportation Electrification

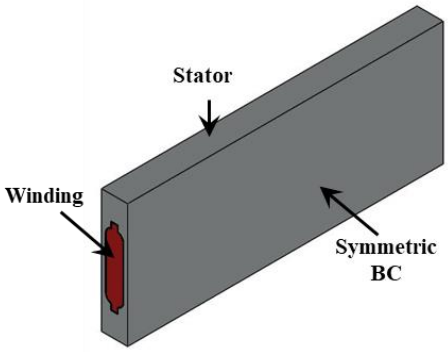

Figure 26: Computation domain and boundary conditions for CFD/HT simulation.

C. Comparison Between Experimental and Numerical Results

Table 5 compares the measured and CFD/HT predicted steady-state average active-winding temperature for different input powers and coolant flow rates. From the table, it can be seen that CFD/HT model can accurately predicts the measured active-winding temperature with a deviation of less than 0.01°C.

Table 5: Comparison of measured and predicted average winding temperature.

Power (W)	Flow rate (mL/min)	Average active-winding temperature (°C)	
		Measured	CFD/HT
702.9	330	113.80	113.80
1106	440	126.82	126.82
1500.7	520	137.40	137.39
1606.3	520	149.10	149.10
1702.9	640	135.20	135.19
2001.6	640	145.20	145.19

Figure 27 shows the measured and predicted transient average active-winding temperature for two different input powers. It can be observed that the measured active-winding temperature agrees well with the predicted temperatures extracted from the CFD/HT model irrespective of the input power. For both input powers, the maximum difference between the measured and predicted temperature was less than 3.4°C.

VIII. Conclusion

This paper examines a novel evaporative cooling (EC) technique confined between the slot liner and active-winding of an electric motor. EC can enhance the heat extraction from the winding by reducing the thermal resistance between the winding and coolant. Most importantly, slot-liner confined EC does not alter the winding copper fill factor, i.e., electro-magnetic (EM) performance, and is applicable in all kinds of electric motor applications, irrespective of the winding configuration. Taking an existing jacket cooled BMW i3 motor as a base case, two-way coupled EM-CFD/HT and EM-LPTN models have been developed to assess the effectiveness of EC

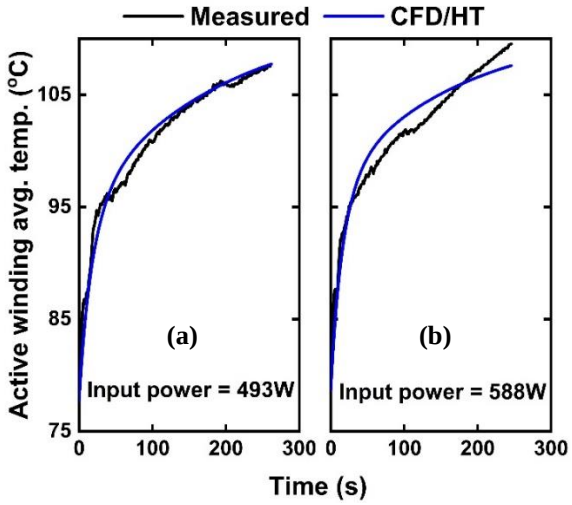

Figure 27: Comparison of measured and predicted average active-winding temperature at total power of (a) 493W and (b) 588W. For both input power, coolant flow rate was 300 mL/min.

over the jacket cooling (JC) for a wide range of current densities. Dielectric coolant FC-84 with a saturation temperature of 80 °C has been considered for EC. Numerical results show that within the insulation thermal limit, and at an evaporative heat transfer coefficient of 5,000 W/m^2.K, EC increases the rms current density by ~78.7% (26 A/mm^2 continuous) compared to the JC and also maintains high electro-thermal efficiency over the JC at any particular current density. Moreover, in case of EC, steady state rms current density can be increased up to 30 A/mm^2, which is about 106.2% higher compared to JC, by using high thermal conductive epoxy impregnation material. Under transient conditions, EC with epoxy impregnation (EC_{EP}) enables 30 s peak rms current density of 40.8 A/mm^2 within the thermal limit of class H insulation. EC and EC_{EP} also exhibit superior thermal performance compared to the JC over a dynamic duty cycle. A 2kW motorette testbed has been designed and fabricated to demonstrate the applicability of the flow assisted EC and to validate the developed CFD/HT model under steady-state and transient conditions. Superior electro-thermal performance and universal applicability of EC makes it a superior cooling technology for the next generation of high power density electric motors.

References

[1] K. T. Chau, C. C. Chan, and C. Liu, "Overview of Permanent-Magnet Brushless Drives for Electric and Hybrid Electric Vehicles," *IEEE Transactions on Industrial Electronics*, vol. 55, no. 6, pp. 2246-2257, 2008.

[2] M. Popescu, D. A. Staton, A. Boglietti, A. Cavagnino, D. Hawkins, and J. Goss, "Modern Heat Extraction Systems for Power Traction Machines—A Review," *IEEE Transactions on Industry Applications*, vol. 52, no. 3, pp. 2167-2175, 2016.

[3] F. JinXin, Z. ChengNing, W. ZhiFu, and E. G. Strangas, "Thermal analysis of water cooled surface mount permanent magnet electric motor for electric vehicle," in *2010 International Conference on*

Electrical Machines and Systems, pp. 1024-1028, 2010.

[4] A. Tikadar, N. Kumar, Y. Joshi, and S. Kumar, "Coupled Electro-Thermal Analysis of Permanent Magnet Synchronous Motor for Electric Vehicles," in *2020 19th IEEE Intersociety Conference on Thermal and Thermomechanical Phenomena in Electronic Systems (ITherm)*, pp. 249-256, 2020.

[5] H. Stiesdal, "Generator with a stator comprising cooling ducts, and method for cooling a laminated stator of a generator," ed: Google Patents, 2013.

[6] A. Tikadar, D. Johnston, N. Kumar, Y. Joshi, and S. Kumar, "Comparison of Electro-Thermal Performance of Advanced Cooling Techniques for Electric Vehicle Motors," *Applied Thermal Engineering*, p. 116182, 2020.

[7] S. A. Semidey and J. R. Mayor, "Experimentation of an Electric Machine Technology Demonstrator Incorporating Direct Winding Heat Exchangers," *IEEE Transactions on Industrial Electronics*, vol. 61, no. 10, pp. 5771-5778, 2014.

[8] I. Petrov, P. Lindh, M. Niemelä, E. Scherman, O. Wallmark, and J. Pyrhönen, "Investigation of a Direct Liquid Cooling System in a Permanent Magnet Synchronous Machine," *IEEE Transactions on Energy Conversion*, vol. 35, no. 2, pp. 808-817, 2020.

[9] A. Acquaviva, S. Skoog, and T. Thiringer, "Design and Verification of In-slot Oil-Cooled Tooth Coil Winding PM Machine for Traction Application," *IEEE Transactions on Industrial Electronics*, pp. 1-1, 2020.

[10] W. Sixel, M. Liu, G. Nellis, and B. Sarlioglu, "Cooling of Windings in Electric Machines via 3D Printed Heat Exchanger," in *2018 IEEE Energy Conversion Congress and Exposition (ECCE)*, 2018, pp. 229-235.

[11] P. Lindh *et al.*, "Direct Liquid Cooling Method Verified With an Axial-Flux Permanent-Magnet Traction Machine Prototype," *IEEE Transactions on Industrial Electronics*, vol. 64, no. 8, pp. 6086-6095, 2017.

[12] C. Rhebergen, B. Bilgin, A. Emadi, E. Rowan, and J. Lo, "Enhancement of electric motor thermal management through axial cooling methods: A materials approach," in *2015 IEEE Energy Conversion Congress and Exposition (ECCE)*, pp. 5682-5688, 2015.

[13] V. Madonna *et al.*, "Improved Thermal Management and Analysis for Stator End-Windings of Electrical Machines," *IEEE Transactions on Industrial Electronics*, vol. 66, no. 7, pp. 5057-5069, 2019.

[14] S. Nategh *et al.*, "Thermal and Manufacturing Aspects of Traction Motors Potting: A Deep Experimental Evaluation," *IEEE Transactions on Energy Conversion*, vol. 35, no. 2, pp. 1026-1035, 2020.

[15] C. Dong *et al.*, "A Review of Thermal Designs for Improving Power Density in Electrical Machines," *IEEE Transactions on Transportation Electrification*, vol. 6, no. 4, pp. 1386-1400, 2020.

[16] T. Hassett and M. Hodowanec, "Electric motor with heat pipes," ed: Google Patents, 2009.

[17] Q. J. Dong and C.-L. Chen, "Motor rotor cooling with rotation heat pipes," ed: Google Patents, 2008.

[18] L. Zhenguo, R. Lin, and T. Longyao, "Heat transfer characteristics of spray evaporative cooling system for large electrical machines," in *2015 18th International Conference on Electrical Machines and Systems (ICEMS)*, pp. 1740-1743, 2015.

[19] K. Bennion, "Electric Motor Thermal Management R&D. Annual Report," National Renewable Energy Lab.(NREL), Golden, CO, United States, 2016.

[20] W. Li and Y. Joshi, "Capillary-Assisted Evaporation/Boiling in PDMS Microchannel Integrated with Wicking Microstructures," *Langmuir*, vol. 36, no. 41, pp. 12143-12149, 2020.

[21] "2016 Annual Progress Report for the Electric Drive Technologies Program," *Oak Ridge National Laboratory (ORNL), TN, United States*, https://www.energy.gov/sites/prod/files/2017/08/f36/FY16%20EDT%20Annual%20Report_FINAL.pdf.

[22] "PDMS Liner Properties," *http://www.mit.edu/~6.777/matprops/pdms.htm*.

[23] "FC-84 Coolant Properties," *3M*, *http://www.reedtec.com/download/FC-84.pdf*.

[24] J. Hu, J. Zou, and W. Liang, "Finite element calculation of the saturation DQ-axes inductance for a direct drive PM synchronous motor considering cross-magnetization," in 2003 *Fifth International Conference on Power Electronics and Drive Systems, PEDS*, vol. 1, pp. 677-681, 2003.

[25] "Ansys Motor-CAD Manual," *https://www.motor-design.com/*.

[26] "N42UH Magnet Properties," *https://www.arnoldmagnetics.com/wp-content/uploads/2017/11/N42UH-151021.pdf*.

[27] R. Wrobel and P. H. Mellor, "A General Cuboidal Element for Three-Dimensional Thermal Modelling," *IEEE Transactions on Magnetics*, vol. 46, no. 8, pp. 3197-3200, 2010.

[28] R. Wrobel, S. J. Williamson, J. D. Booker, and P. H. J. I. T. o. I. A. Mellor, "Characterizing the in situ thermal behavior of selected electrical machine insulation and impregnation materials," vol. 52, no. 6, pp. 4678-4687, 2016.

[29] N. Simpson, R. Wrobel, and P. H. Mellor, "Estimation of Equivalent Thermal Parameters of Impregnated Electrical Windings," *IEEE Transactions on Industry Applications*, vol. 49, no. 6, pp. 2505-2515, 2013.

[30] Y. Shi, J. B. Wang, and B. Wang, "Transient 3D Lumped Parameter and 3D FE Thermal Models of a PMASynRM under Fault Conditions with Asymmetric Temperature Distribution," *IEEE Transactions on Industrial Electronics*, pp. 1-1, 2020.

[31] "Epoxy Encapsulant Properties," *https://www.lord.com/products-and-solutions/electronic-materials/cooltherm-ep-2000-thermally-conductive-epoxy-encapsulant*.

Amitav Tikadar (Student Member, IEEE) received his B.S and MS degree in mechanical engineering from Bangladesh University of Technology (BUET), Bangladesh and University of South Carolina, USA, in 2015 and 2019, respectively. He is currently pursuing his PhD degree in mechanical engineering at Georgia Institute of Technology, USA. His research interest focuses on electric machine thermal management, micro-scale heat transfer, and machine learning.

Joon Woo Kim (Student Member, IEEE) received the bachelor's degree from University of Missouri, Columbia, MO, USA, in 2017, and the master's degree from University of California, Berkeley, CA, USA, in 2018, both in mechanical engineering. He was pursuing the Ph.D. degree in mechanical engineering with the Microelectronics and Emerging Technologies Thermal Lab, Georgia Institute of Technology, Atlanta, GA, USA. Since 2021, he is pursuing the PhD degree in electrical engineering degree with the 3D Systems Packaging Research Center, Georgia Institute of Technology, USA. His research interests include thermal analysis, thermal management of electronics, electric machine design, and the temperature prediction of electric machines.

Yogendra Joshi (Fellow, IEEE) is Professor and John M. McKenney and Warren D. Shiver Distinguished Chair at the G.W. Woodruff School of Mechanical Engineering at the Georgia Institute of Technology. His research interests are in multi-scale thermal management. He is the author or co-author of nearly four hundred publications in this area, including nearly two hundred journal articles. He received his B. Tech. in Mechanical Engineering from the Indian Institute of Technology (Kanpur) in 1979, M.S. in Mechanical Engineering from the State University of New York at Buffalo in 1981, and Ph.D. in Mechanical Engineering and Applied Mechanics, from the University of Pennsylvania in 1984. He has served as the Principal Investigator for multiple Defense Advanced Research Projects Agency (DARPA) programs, and Office of Naval Research Consortium for Resource-Secure Outposts (CORSO). He was Site Director for the National Science Foundation Industry/University Cooperative Research Center on Energy Efficient Electronic Systems. He has held visiting faculty appointments at Stanford University, Katholieke Universiteit Leuven, and Xi'an Jiaotong University. He is an elected Fellow of the ASME, the American Association for the Advancement of Science, and IEEE. He was a co-recipient of ASME Curriculum Innovation Award (1999), Inventor Recognition Award from the Semiconductor Research Corporation (2001), the ASME Electronic and Photonic Packaging Division Outstanding Contribution Award in Thermal Management (2006), ASME J. of Electronics Packaging Best Paper of the Year Award (2008), IBM Faculty Award (2008), IEEE SemiTherm Significant Contributor Award (2009), IIT Kanpur Distinguished Alumnus Award (2011), ASME InterPack Achievement Award (2011), ITherm Achievement Award (2012), ASME Heat Transfer Memor.

Satish Kumar (Senior Member, IEEE) is currently Professor in George W. Woodruff School of Mechanical Engineering at Georgia Tech. Prior to joining Georgia Tech in 2009 as an Assistant Professor, he worked at IBM Corporation where he was responsible for the thermal management of electronic devices. Kumar received his Ph.D. in Mechanical Engineering and M.S. degree in Electrical and Computer Engineering from Purdue University, West Lafayette in 2007; and B.Tech. degree in Mechanical Engineering from the Indian Institute of Technology, Guwahati in 2001. His research interests are in electro-thermal transport study in electronic devices/materials, wide band-gap devices, and flexible-electronics. He is author or co-author of over 100 journal or conference publications. He is an ASME Fellow and a Woodruff Faculty Fellow. He is an recepient of 2005 Purdue Research Foundation Fellowship, 2012 Summer Faculty Fellow from Air Force Research Lab, 2014 Sigma Xi Young Faculty Award, 2014 DARPA Young Faculty Award, and 2020 ASME K16 Clock Award.